A 3D hybrid DFPM-DFM Model for gas production from fractured shale reservoirs

Jianwei Tian [a,*], Jishan Liu [a], Derek Elsworth [b], Yee-Kwong Leong [a]

[a] School of Engineering, The University of Western Australia, 35 Stirling Highway, WA 6009, Australia
[b] Department of Energy and Mineral Engineering, G3 Centre and Energy Institute, The Pennsylvania State University, University Park, PA 16802, USA

ABSTRACT

Hydraulic fracturing as a key technology has been applied to improve gas productivity from shale reservoirs. Both induced hydraulic fractures (HFs) and inherent natural fractures (NFs) delineate a shale reservoir into matrix and fracture domains. Accurate characterizations of matrix and fracture are critical in evaluating gas production. In this work, an in-house built 3D discrete fracture model (DFM) was proposed to explicitly represent the distribution of the NFs network. Gas flow in shale matrix containing multiscale pores in inorganic matters (IOM) and organic matters (OM) was represented by a dual-fractal permeability model (DFPM). Consequentially, a hybrid DFPM–DFM model was proposed to couple gas flow and geomechanics the model was solved by commercial software based on the finite element method. The proposed model was verified using field data from a shale reservoir. The model was further employed to investigate the impacts of fractally-distributed pore size and fracture attributes on the evolutions of permeability and the associated gas production. The results showed that the fractally distributed pore size of IOM accounts for the diverse profiles of permeability evolution that exhibits a downward trend before rebounding. The impacts of pore diameter and tortuosity index on cumulative gas production were quantitatively analysed. We also highlighted the remarkable effects of fracture patterns (fracture connectivity, aperture and number) on cumulative gas production. This work provides a framework to explore the multiscale structural heterogeneities on hydrocarbon recovery and shale deformation.

1. Introduction

Hydrocarbons extracted from shale reservoirs have become a significant supplement to the natural gas industry (Wang and Krupnick, 2015). Primitive shale reservoirs have strong heterogeneity and ultra-low permeability (Chen et al., 2015; Wang et al., 2016; Wu et al., 2019). The application of hydraulic fracturing stimulates the reservoir by creating multistage hydraulic fractures (HFs), which enable the commercial exploitation of shale gas (Clarkson et al., 2011). Well-developed HFs come into contact with inherent natural fractures (NFs) to produce interconnected fracture networks (Jamison and Azad, 2017). These constructed fracture networks segment the shale into matrix and fracture domains. The matrix domain acts as a storage place for the shale gas, while the fractures serve as preferential flow channels for the gas outflow. An accurate conceptual understanding of gas transport in shale matrices and the characterization of shale fracture networks are still the main challenges in modelling and forecasting shale-gas production.

A shale matrix is composed of organic matter (OM) and inorganic matter (IOM), with abundant micropores in both. The effect of rarefaction is prominent and the flow regimes are versatile. Slip flow is presumed to be the primary reason for discrepancies between experimentally-measured permeability and the intrinsic permeability predicted by continuum flow (Beskok and Karniadakis, 1999; Civan, 2010). Javadpour (Javadpour, 2009) argued that viscous flow and Knudsen diffusion coexist in nanopores. Following this, surface diffusion was also included in apparent permeability models (Cao et al., 2016b; Kang et al., 2011). The multiple flow regimes are directly correlated with pore size. Hence, fractal-based permeability models have been developed to incorporate the pore size distribution (Cai et al., 2018; Geng et al., 2016; Hu et al., 2020). Besides the dual-porosity model, triple-porosity (OM, IOM and NFs) models have been proposed to incorporate the effects of NFs based on the assumption that the fracture system is a continuum (Huang et al., 2015; Sang et al., 2016; Wang et al., 2018a). However, because NFs are non-uniformly distributed in shales, the interaction between NFs and HFs cannot be captured by continuum models. Therefore, accurate characterization of pre-existing fractures is

a prerequisite to forecast shale-gas production.

The discrete fracture model (DFM) has become an effective approach in characterizing the realistic and complex geometries of rock fractures, applicable to both single-phase and two-phase flow scenarios (Lei et al., 2017; Ma et al., 2021). Application of 2D discrete fracture network enables the incorporation of outcrop trace map of fractures in simulations, but it has been found that the hydraulic conductivity would be underestimated compared with 3D models (Berkowitz and Adler, 1998; Lang et al., 2014). In the modelling based on 3D DFM, fractures are explicitly represented by two-dimensional planes without thickness. The attributes of a fracture network are crucial for the enhancement of gas productivity. As one of its distinctive properties, a favourable fracture connectivity between NFs can remarkably improve the overall permeability. Moreover, when artificially-generated HFs are connected with pre-existing NFs, an expanded stimulated reservoir volume can be created. Based on an DFM, Makedonskaet al. (Makedonska et al., 2020a) investigated the impacts of interactions between HFs and NFs on gas production. According to the study of Li et al. (Li et al., 2018), the HF–NF interaction points and effective fracture density were the dominant factors in determining the ultimate recovery, further highlighting the importance of fracture connectivity.

The present study aimed to explore the influences of multiscale structural heterogeneities on gas production rates in shale reservoirs within the context of fluid–solid coupling. To this end, a hybrid dual-fractal permeability model (DFPM) and discrete fracture model (DFM) was employed to capture the complex multiscale pore size distributions (OM and IOM) and fracture networks (NFs and HFs) in shale reservoirs. In comparison to prior studies that employed fractal-based models and DFMs (Cai et al., 2018; Sheng et al., 2016; Wang et al., 2015), this study advanced the state of the art by incorporating the impacts of effective stress and multiple flow mechanisms in the simulation. This was achieved through the implementation of an effective stress-dependent multiscale fractal structure and fracture permeability model, allowing for the dynamic evolution of multiscale heterogeneities to be captured during gas depletion. The resultant hybrid model delivers superior predictions for shale gas production and offers a more comprehensive understanding of the dynamic evolution of structural heterogeneity under effective stress.

The geomechanics and multiscale gas transport were coupled through the evolutions of porosity and permeability. Fig. 1 shows the conceptual model for the proposed model. The integrated model was solved using the finite element method. The developed dual-fractal permeability model was verified against experimental data, and the coupled DFPM–DFM model was verified using field data. The associated impacts of fractal parameters on permeability and gas production were investigated, while the implications of fracture properties—including HF spacing, NF connectivity and fracture apertures—on gas production were evaluated through reservoir simulation.
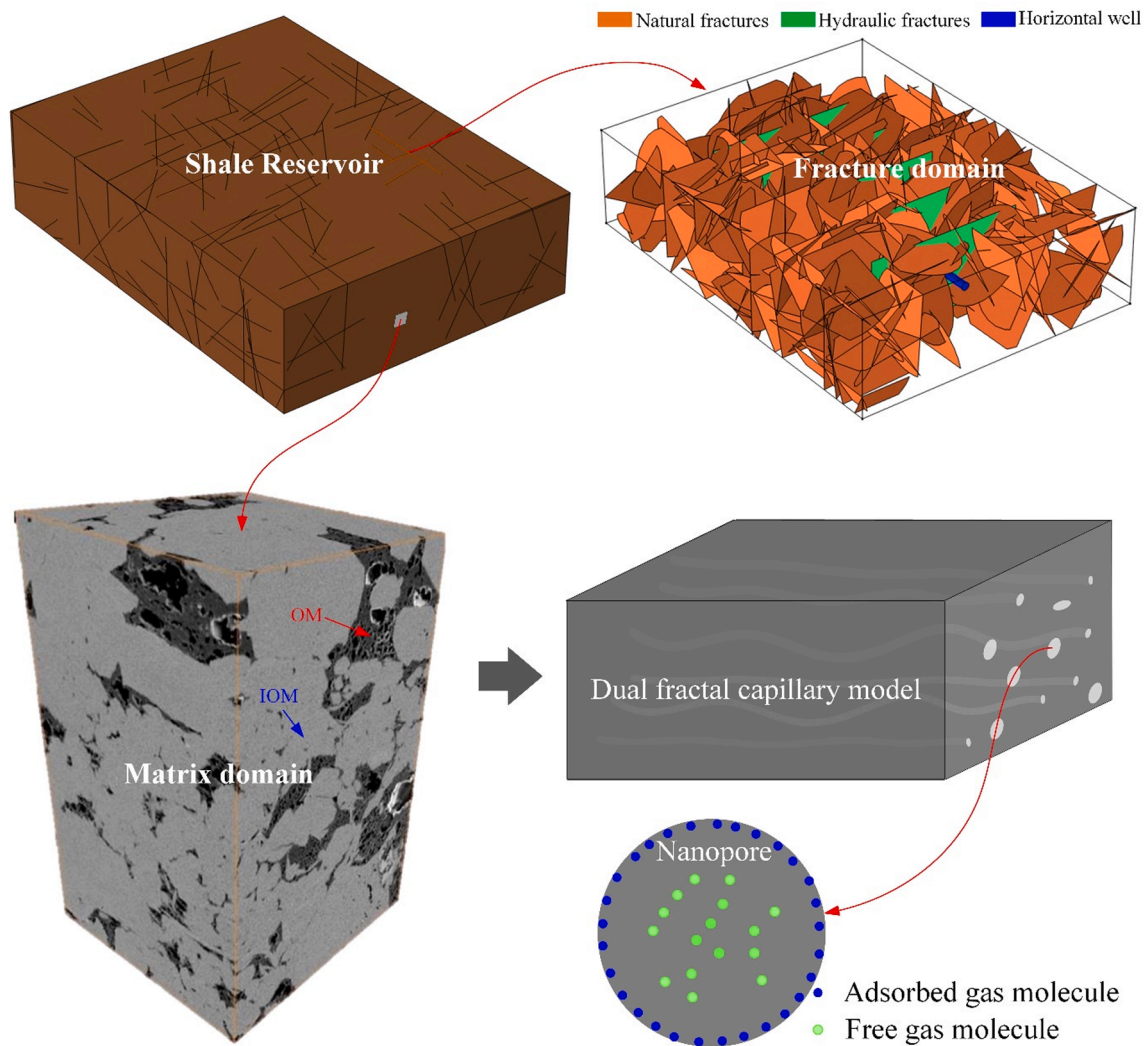

Fig. 1. Schematic illustration of the discrete fracture network for shale reservoir (SEM image of shale matrix domain is from Almarzooq, et al. (Almarzooq et al., 2014)).

2. Model development

2.1. Governing equations for the shale deformation

In this study, the shale matrix comprised of OM and IOM is treated as a dual-porosity system, indicating that its seepage properties and mechanical properties are different. Specifically, it is necessary to represent the pore pressure and bulk modulus individually in the model formulation. Based on the poroelastic theory, the constitutive equation for shale deformation is expressed as (Cao et al., 2016a; Zhang et al., 2008):

$$\varepsilon_{ij} = \frac{1}{2G}\sigma_{ij} - \left(\frac{1}{6G} - \frac{1}{9K_t}\right)\sigma_{KK}\delta_{ij} + \frac{\alpha_m p_m}{3K_m}\delta_{ij} + \frac{\alpha_k p_k}{3K_k}\delta_{ij} + \frac{\varepsilon_s}{3}\delta_{ij} \tag{1}$$

where ε_{ij} and σ_{ij} are the component of the total strain tensor and total stress tensor respectively; G and K_t are the shear modulus and bulk modulus of shale; $\sigma_{KK} = \sigma_{11} + \sigma_{22} + \sigma_{33}$; δ_{ij} is the Kronecker delta; ε_s is the sorption-induced volumetric strain; α_m is the Biot coefficient of the shale inorganic matrix; p_m is the pore pressure in shale inorganic matrix; α_k is the Biot coefficient of the shale kerogen; p_k is the pore pressure in shale kerogen system. The swelling strain can be derived using the extended Langmuir equation, expressed as (Shi and Durucan, 2004):

$$\varepsilon_s = \frac{\varepsilon_L p_k}{P_L + p_k} \tag{2}$$

where ε_L is the Langmuir volumetric strain constant, P_L is the Langmuir pressure constant and p_k is the pore pressure in the kerogen system.

The first and second terms correspond to the normal and shear strains induced by the stress tensor, respectively; the third and fourth terms represent the strains arising from gas pressure in the kerogen system and inorganic matrix; the last term denotes the sorption-induced strain.

For the homogeneous, isotropic and elastic medium, the constitutive relation describing strain–displacement is expressed as:

$$\varepsilon_{ij} = \frac{1}{2}\left(u_{i,j} + u_{j,i}\right) \tag{3}$$

where ε_{ij} is the component of the total strain tensor and u_i is the component of the displacement. The equilibrium equation is defined as:

$$\sigma_{ij,j} + f_i = 0 \tag{4}$$

f_i denotes the component of the body force. The Navier equation can be obtained by combining the Eqs. (1), (3) and (4), as follows:

$$Gu_{i,kk} + \frac{G}{1-2\nu}u_{k,ki} - \alpha_k p_{k,i} - \alpha_m p_{m,i} - K\varepsilon_{s,i} + f_i = 0 \tag{5}$$

2.2. Governing equations for the gas flow in shale matrix

2.2.1. Governing equations for gas flow in kerogen

In the shale matrix, gas exits as adsorbed gas and free gas. During gas depletion process, gas transfers from matrix to fracture network. The mass balance equation for shale gas flow in the matrix is expressed as:

$$\frac{\partial m_k}{\partial t} + \nabla \cdot \left(-\rho_k \frac{k_k}{\mu}\nabla p_k\right) = -Q_{mk} \tag{6}$$

where m_k denotes the total gas content in shale matrix, which includes the free gas in nanopores and adsorption gas, k_k is the permeability of matrix, Q_{mk} on the right side of the equation is the source term. As in kerogen system, the total gas content is composed free gas and adsorbed gas, which is determined as:

$$m_k = \rho_{gk}\phi_k + \rho_{ga}\rho_s \frac{V_L p_k}{p_k + P_L} \tag{7}$$

where ρ_{gk} is gas density in the kerogen system at corresponding pressure,

ϕ_k is the porosity of kerogen, ρ_{ga} is the gas density at standard conditions, ρ_s denotes the density of the solid matrix, V_L and P_L denote the Langmuir volume and Langmuir pressure constant. The equivalent permeability of shale matrix is determined in previous study (Tian et al., 2022; Tian et al., 2019):

$$k_k = \underbrace{\frac{\pi}{128}\frac{\phi_k D_{ho}}{3 + D_{To} - D_{ho}}\frac{h_{maxo}^{3+D_{To}}}{L_0^{D_{To}+1}}}_{\text{viscous flow}} + \underbrace{\sqrt{\frac{2\pi RT}{M_g}}\frac{\phi_k \mu D_{ho}}{(2 + D_{To} - D_{ho})}\frac{h_{maxo}^{2+D_{To}}}{6p_k L_0^{D_{To}+1}}}_{\text{Knudsen diffusion}}$$
$$+ \underbrace{\frac{\pi D_s P_L C_{us} RT}{(p_k + P_L)^2 p_k}\frac{\mu D_{ho}}{(2 + D_{To} - D_{ho})}\frac{h_{maxo}^{1+D_{To}}}{L_0^{D_{To}+1}}}_{\text{Surface diffusion}} \tag{8}$$

where D_{ho} is the fractal dimension of pore size distribution OM; D_{To} is the fractal dimension of tortuosity of OM pores; h_{maxo} is the maximum pore diameter of OM; L_0 the characteristic length of REV. Under the impact of effective stress, the effective porosity of kerogen system is calculated by the Cui-Bustin model (Cui and Bustin, 2005):

$$\frac{\phi_k}{\phi_{k0}} = \exp\{-c_k[(\overline{\sigma} - \overline{\sigma}_0) - (p_k - p_{k0})]\} \tag{9}$$

where ϕ_{k0} is the initial porosity; $\overline{\sigma}$ and $\overline{\sigma}_0$ are the current mean total stress and initial mean total stress; p_{k0} is the initial pore pressure in kerogen; C_k denotes the bulk compressibility of kerogen system.

The maximum pore diameter (MPD) can be determined based on the previous paper (Tian et al., 2023; Tian et al., 2022):

$$\frac{h_{maxo}^3}{h_{maxo0}^3} = \left[1 + \frac{\alpha_k}{\phi_k}(S - S_0) - \frac{p_k - p_0}{K_s} + \varepsilon_s - \varepsilon_{s0}\right]\frac{3 - D_{ho}}{3 - D_{ho0}}\frac{D_{ho0}}{D_{ho}}\frac{1 - \phi_{k0}}{1 - \phi_k} \tag{10}$$

where h_{maxo} is the MPD of OM, h_{maxo} is the initial MPD of IOM, $S = \varepsilon_v + \frac{p_k}{K_s} - \varepsilon_s$, $S_0 = \varepsilon_{v0} + \frac{p_0}{K_s} - \varepsilon_{s0}$, $D_{ho} = 3 - \ln\phi_k/\ln h_{minio}/h_{maxio}$, $\varepsilon_v = \varepsilon_{11} + \varepsilon_{22} + \varepsilon_{33}$ is the volumetric strain of shale matrix, K_s is the bulk modulus of shale OM, D_{ho0} is the initial fractal dimension of OM, and in this study, the ratio of h_{minio}/h_{maxio} is kept constant.

2.2.2. Governing equations for gas flow in inorganic matrix

The mass balance equation for gas flow in IOM is expressed a:

$$\frac{\partial m_m}{\partial t} + \nabla \cdot \left(\rho_{gm}\boldsymbol{q}_{gm}\right) = Q_{mk} \tag{11}$$

where m_m is the free gas content within the IOM, defined as $m_m = \rho_{gm}\phi_m$, where ρ_{gm} represents the density of free gas within the IOM defined as an ideal gas as $\rho_{gm} = Mp_m/RT$, $\boldsymbol{q}_{gm}$ is the Darcy velocity vector, with $Q_{mk} = a\rho_{gk}k_k/\mu(p_k - p_m)$, representing a source term for gas transfer between OM and IOM, a is the shape factor. Therefore, Eq. (9) can be rewritten as:

$$\phi_m\frac{\partial\rho_{gm}}{\partial t} + \rho_{gm}\frac{\partial\phi_m}{\partial t} - \nabla \cdot \left(\frac{k_m}{\mu}\rho_{gm}\nabla p_m\right) = a\rho_{gk}k_k/\mu(p_k - p_m) \tag{12}$$

The apparent permeability of IOM is expressed as:

$$k_m = \frac{\pi}{128}\frac{\phi_m D_{hi}}{3 + D_{Ti} - D_{hi}}\frac{h_{maxi}^{3+D_{Ti}}}{L_{m0}^{D_{Ti}+1}}\left(1 + \frac{8\mu(3 + D_{Ti} - D_{hi})}{h_{maxi}p_m(2 + D_{Ti} - D_{hi})}\sqrt{\frac{\pi RT}{2M_g}}\right) \tag{13}$$

where D_{hi} is the fractal dimension of the PSD in the IOM, h_{maxi} is the MPD within the IOM. The evolution of inorganic matrix porosity and pore diameter h under effective stress is calculated using the Cui-Bustin model (Cui and Bustin, 2005):

$$\frac{\phi_m}{\phi_{m0}} = \exp(-c_m[\overline{\sigma} - \overline{\sigma}_0 - (p_m - p_{m0})]) \tag{14}$$

where ϕ_{m0} is the initial porosity of IOM; $\overline{\sigma}$ and $\overline{\sigma}_0$ are the current mean total stress and initial mean total stress; p_{m0} is the initial pore pressure in

kerogen; C_m denotes the bulk compressibility of IOM. As it is assumed that there is no gas adsorption in the IOM, therefore, the MPD is only affected by the effective stress, which is expressed as:

$$\frac{h_{\max i}^3}{h_{\max i0}^3} = \left[1 + \frac{\alpha_m}{\phi_m}\left(\varepsilon_v - \varepsilon_{v0} + \frac{p_m - p_0}{K_m}\right) - \frac{p_m - p_0}{K_m}\right]\frac{3 - D_{hi}}{3 - D_{hi0}}\frac{D_{hi0}}{D_{hi}}\frac{1 - \phi_{m0}}{1 - \phi_m}$$

(15)

where $h_{\max i}$ is the MPD of IOM, $h_{\max i0}$ is the initial MPD of IOM, $\varepsilon_v = \varepsilon_{11} + \varepsilon_{22} + \varepsilon_{33}$ is the volumetric strain of shale matrix, K_m is the bulk modulus of shale IOM, D_{hi} is the fractal dimension of PSD in shale IOM, $D_{hi} = 3 - \ln\phi_m/\ln h_{\min i}/h_{\max i}$, D_{hi0} is the initial fractal dimension of IOM, and in this study, the ratio of $h_{\min i}/h_{\max i}$ is kept constant.

2.3. Governing equations for gas flow in the discrete fracture network

The gas flux transport through the fracture channel is calculated using fracture Darcy's law, which is expressed as:

$$\boldsymbol{q}_f = -\frac{k_f}{\mu}d_f\nabla_T p_f$$

(16)

where $\boldsymbol{q}_f$ are the rate of gas flow through the unit length of HFs and NFs, d_f is the fracture aperture, k_f denotes the fracture permeability, and $\nabla_T p_f$ is the pressure gradient in the tangential direction of HF and NF domain. The mass conservation in the fracture follows the equation (Cao et al., 2016b):

$$d_f\frac{\partial(\phi_f\rho_f)}{\partial t} + \nabla_T\cdot(\rho_f\boldsymbol{q}_f) = 0$$

(17)

where ϕ_f denotes the fracture porosity, ρ_f is the gas density in the fracture network. The fractures in COMSOL are treated as thin elastic layers with independent normal and shear stiffness. Therefore, the force exerted by geomechanics on fractures is calculated by the equation below:

$$\boldsymbol{F}_A = -\boldsymbol{k}_A(\boldsymbol{u}_u - \boldsymbol{u}_d - \boldsymbol{u}_0) - \boldsymbol{d}_A\frac{\partial(\boldsymbol{u}_u - \boldsymbol{u}_d - \boldsymbol{u}_0)}{\partial t} - \frac{1}{2}\rho_f b\frac{\partial^2(\boldsymbol{u}_u + \boldsymbol{u}_d)}{\partial t^2}$$

(18)

where $\boldsymbol{F}_A$ is a force/unit area, $\boldsymbol{u}_u$ and $\boldsymbol{u}_d$ are the "upside" and "downside" displacement, respectively, $\boldsymbol{d}_A$ is the damping constant per unit area, ρ is the fracture density, b is the thickness fractures, $\boldsymbol{k}_A$ is the total stiffness matrix and is defined as follows:

$$\boldsymbol{k}_A = k_n\boldsymbol{n}\otimes\boldsymbol{n} + k_s(\boldsymbol{I} - \boldsymbol{n}\otimes\boldsymbol{n})$$

(19)

where k_n and k_s are the normal and shear stiffness of the fracture plane, respectively, $\boldsymbol{I}$ is the unity tensor, $\boldsymbol{n}$ is the unit normal vector of the fracture plane, and the normal and shear stiffness are defined as:

$$k_n = \frac{E_f(1 - v_f)}{b(1 + v_f)(1 - 2v_f)}, \quad k_S = \frac{E_f}{2b(1 + v_f)}$$

(20)

Where E_f, v_f, and b denote the elasticity modulus, Poisson's ratio and fracture thickness. When the reservoir is depleted, the permeability of the fracture network decreases simultaneously alongside the variation of effective stress. Under the triaxial-stress condition, the fracture permeability is mainly dependent on the fluctuation of normal effective stress (Barton et al., 1985; Chang et al., 2004; Li et al., 2021). In this work, the evolution of fracture permeability with the variation of pore pressure takes the form of (Miller, 2012; Rice, 1992):

$$k_f = k_{f0}\exp(-\gamma\sigma_n')$$

(21)

where k_f is fracture permeability, k_{f0} is the initial fracture permeability, $\sigma_n' = \sigma_n - \alpha p$ is the effective normal stress, γ is the normalizing constant, which physically represents the fracture compressibility (Li et al., 2021). Therefore, the permeability for HFs and NFs can be obtained as:

$$k_f = k_{f0}\exp(-c_f(\Delta\sigma_n - \Delta p))$$

(22)

where k_{f0} denotes the initial permeability of fractures, c_f is the compressibility of fractures, σ_n is the normal stress.

3. Model Implementation

3.1. Generation of 3D discrete natural fracture network

The complex fracture network of a shale reservoir was generated explicitly using the Monte Carlo method, which divided the shale reservoir into a discrete rock matrix of tetrahedral elements. Based on the Baecher disc model, the NFs were presented as circle planes. The centre points of the fractures were uniformly distributed in the study domain, and the dip angle and direction followed a Fisher distribution. The NF Network, HFs and matrix domains were generated in MATLAB and then imported into COMSOL Multiphysics (a finite-element, method-based PDE solver) for further modelling. COMSOL performs tetrahedral meshing on the calculation domain based on the Delaunay tetrahedron, embedding the zero-thickness planes in the study domain. The fractured shale reservoir was discretised as tetrahedral elements for the shale matrix and as triangular elements for the discrete fractures.

3.2. Solution of the multi-physics coupling model

Previous equations governing multiscale gas flow and shale deformation, along with cross-coupling equations, were implemented in COMSOL Multiphysics. Interaction between the shale matrix and fracture network was achieved through the gas exchange, which is dependent on diffusivity and a shape factor. It should be noted that, for this study, the shale matrix was assumed to be a dual-porosity medium, with a multiscale-pore-size distribution that followed fractal scaling law. Therefore, the modules for subsurface flow and structural mechanics were used to compute the governing and cross-coupling equations. The fracture flow module was used to compute gas transport in the HFs and NFs.

4. Model verification

4.1. Matrix permeability verification against experimental data

The apparent permeability of the matrix was first verified using two sets of experimental data from published sources. As in this study, the shale matrix in these experimental datasets was assumed to be a dual continuum, so an apparent permeability had to be calculated to match these experimental data. According to previous studies (Shi et al., 2013; Wang et al., 2018b), the apparent permeability can be determined by weighting the OM and IOM permeability based on the total organic carbon (TOC), which can be calculated by:

$$k_{app} = \omega k_k + (1 - \omega)k_{in}$$

(23)

where k_{app} is the apparent permeability of the shale matrix, k_k is the permeability of OM, while k_{in} is the permeability of IOM, and ω is the volume percentage of TOC. Effective stress was not included, thus the permeability evolved with the pore pressure. For the OM, the apparent permeability was a superposition of the viscous flow, and Knudsen and surface diffusion. The apparent permeability of the viscous flow remained constant when the pore pressure declined, while the Knudsen diffusion and surface diffusion were inversely proportional to the pore pressure. Therefore, the decrease in pore pressure triggered the increase in the apparent permeability of OM. By contrast, due to the impact of slip flow in IOM, the apparent permeability of the viscous flow also scaled up when the pore pressure declined. In Eqs. (8) and (13), the OM and IOM permeability are pressure-dependent, provided that the relevant structure parameters, namely fractal dimension, maximum pore

diameter, and minimum pore diameter, were obtained through experiment as reported in the original literature (Letham, 2011; Tinni et al., 2012). Consequentially, the evolution of permeability against pressure in the proposed model was determined based on MATLAB. The experimental data from a core sample of Barnett Shale (Letham, 2011) and a crushed sample of Haynesville Shale (Tinni et al., 2012) were selected to verify the robustness of the proposed dual-fractal-matrix permeability model. The parameters used for the verification are listed in Table 1. As shown in Fig. 2, profiles of the evolution of permeability agree well with the experimental data. It can be seen that the apparent permeability of the Barnett Shale is much greater than that of the Haynesville Shale, which can possibly be credited to the relatively smaller pore size. The MPD from Letham (2011) is 250 nm, while for the core sample from Tinni et al. (2012), it is 100 nm. The TOC in the Haynesville Shale is 4%, which is greater than the 0.77% in the core sample from Letham (2011), indicating that the contribution of OM permeability to the total apparent permeability is greater than that of the Barnett Shale.

4.2. Model verification against field data

The model was verified using field data from Haynesville Shale. The reservoir was assumed to be a cuboid, with dimensions of 200 × 200 × 200 m. A horizontal well was drilled perpendicular to the HF plane, with a well radius of 0.1 m. The initial reservoir pressure was set as 60 MPa, while the bottom-hole pressure in the wellbore was 20 MPa. The pressure differential between the bottom of the hole and the reservoir promoted gas transport from the shale matrix to the fracture network, and ultimately the wellbore. The fracture configuration, including HFs and NFs, was based on published sources (Karra et al., 2015). The orientations of NFs and HFs are presented in Fig. 3. The other parameters used for the simulation were obtained from the literature (Karra et al., 2015; Yu and Sepehrnoori, 2014). The fractal parameters were estimated based on the permeability and porosity values. Fig. 4 is a schematic representation of the physical model for verification. The intersected boundaries of the horizontal well and HFs were set as the bottom hole pressure, while the other boundaries were set as no-flow boundaries. No stress boundary was applied to the boundaries. The other parameters are listed in Table 2 and the simulation time was 1800 days. The simulation was completed on the platform of Intel(R) Xeon(R) Platinum 9242 CPU, 2.30 GHz, 64 cores, RAM 384 GB. The total simulation time is 2 h 46 min.

A comparison of the simulated production data and the field data is presented in Fig. 5, which includes the gas rate and cumulative gas production. It should be noted that the modelling results replicated the real production data well, except for a discrepancy at the beginning of gas depletion, which can be attributed to the skin effect. Moreover, the gas rate and cumulative gas production were slightly higher than the field data, which possibly indicates a disregard for the closure of the fracture network. It can be seen that the gas production rate plunged in

the first 400 days, decreasing from 2.25×10^5 to 5×10^4 m^3/day. After that, the gas production rate experienced a slow descent. In the early stage of gas depletion, the artificially-generated HFs and pre-existing NFs stimulated the reservoir volume, which dramatically accelerated the gas recovery. However, in the later stage, the matrix permeability dominated the gas production rate, producing the long tail production. The spatial distributions of IOM pressure are presented in Fig. 6 for production times of 10, 100, 1000 and 1800 days. Firstly, the gas in the HFs and NFs flowed into the horizontal well, initiating a propagation pressure wave. Based on this, the pressure difference caused the gas stored in the matrix to desorb from the pore surfaces and diffuse into the fracture system. The drainage area expanded continuously, correlating with a rapid decline in the pre-pressure, as depicted in Fig. 5.

5. Sensitivity analysis

In this section, a base case model was established to perform sensitivity analysis, with the basic parameters listed in Table 2. The reservoir was assumed to be a cuboid, with dimensions of 150 × 150 × 150 m. A horizontal well was drilled perpendicular to the HF plane, with a well radius of 0.1 m. The initial reservoir pressure was set as 20.34 MPa, while the bottom-hole pressure in the wellbore was 2 MPa. The base case contained 50 NFs and five HFs in the simulation geometry to reduce the computing time. Fig. 7 depicts the pole plot and contour for dip and strike distributions. The NFs and HFs were treated as thin elastic layers with independent normal and shear stiffness. The gas adsorption and effective stress were included in the modelling. The left, right and vertical boundaries are stress-controlled boundaries. The bottom surface is considered a fixed boundary and the other boundaries are roller constrained, as shown in Fig. 8. The simulation is completed in the same platform as the field verification. The total simulation time for the base case is 55 min.

The base case is a fully coupled DFPM-DFM model for shale gas production. Fig. 9 depicts the spatial and temporal evolutions of reservoir pressure, stress and shale matrix permeability. In the early days (t = 10 days), the fracture plane and the surrounding domain witness a rapid pressure decline, with pressure decreasing to approximately 12 MPa. At this time the mean effective stress exhibits a heterogeneous distribution. The mean effective stress in the vicinity of the stress-controlled boundary (high-stress zone) shows a higher value than that in the roller-controlled boundary (low-stress zone). Correspondingly, the matrix permeability of the high-stress zone is larger than that in the low-stress zone. As the pressure difference propagates to the matrix, the pressure in the shale matrix declines rapidly. When the production time comes to t = 100 days, the near-fracture pressure drops below 6 MPa while the matrix pressure drops from 20 MPa to 15 MPa. Meanwhile, the mean effective stress in the high-stress zone reaches 40 MPa. The matrix permeability experiences a minor change, with 4×10^{-19} m^2 in the high-stress zone and 4.5×10^{-19} m^2 in the low-stress zone. When the matrix pressure in the further region of fracture-matrix interfaces drops below 10 MPa (t = 1000 days), the pressurization migrates to the whole simulation domain.

5.1. Impacts of multiple mechanisms

The presence of NFs in the shale reservoir segmented the shale matrix into smaller sizes, increasing the surface area and accelerating gas transfer between the matrix and the fracture. However, the OM and IOM are the major storage places for shale gas while the fracture network serves as the primary flow pathway. This work considers gas adsorption, geomechanics and multiscale structural heterogeneity. To clarify the importance of multiple mechanisms, four scenarios of the simulation were performed, with NFs (as the base case), without NFs, without adsorption phenomena and the geomechanics. As shown in Fig. 10, the presence of NFs plays the most significant role in the gas production rate. At the early time of gas production (t = 200 days), the scenario
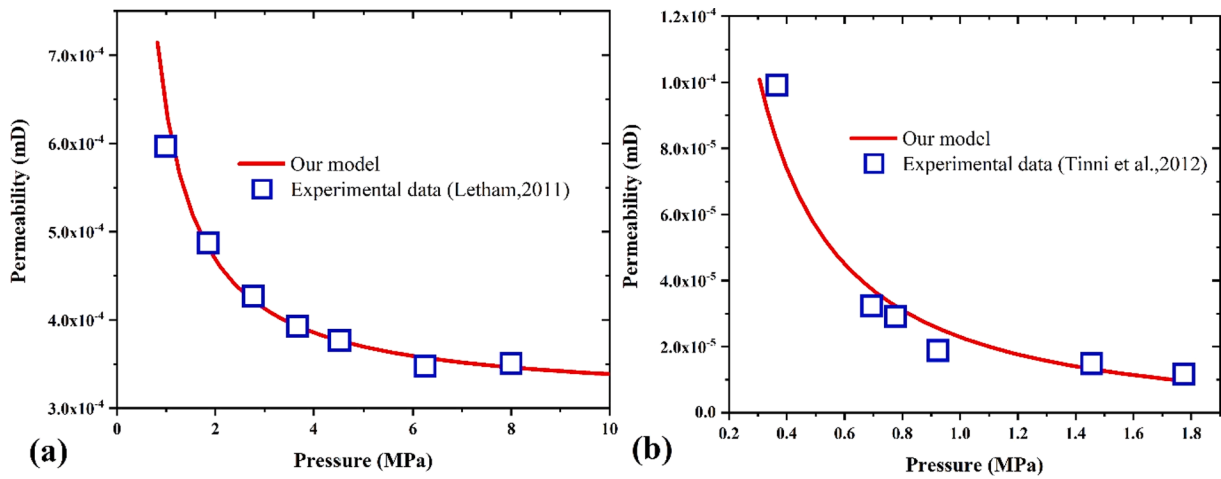
Table 1

The Parameters used in the permeability verification.

Parameters	Organic matters	Inorganic matters	Unit
Properties of Barnett shale			
Fractal dimension of PSD	2.1	2.3	
Fractal dimension of tortuosity	1.3	1.3	
Porosity	0.03	0.05	
MPD	50	250	nm
Minimum pore diameter	1	1	nm
TOC	0.77%	—	
Properties of Hayneville shale			
Fractal dimension of PSD	1.8		
Fractal dimension of tortuosity	1.6	1.6	
Porosity	0.01	0.008	
MPD	50	100	nm
Minimum pore diameter	1	1	nm
TOC	4%	—	

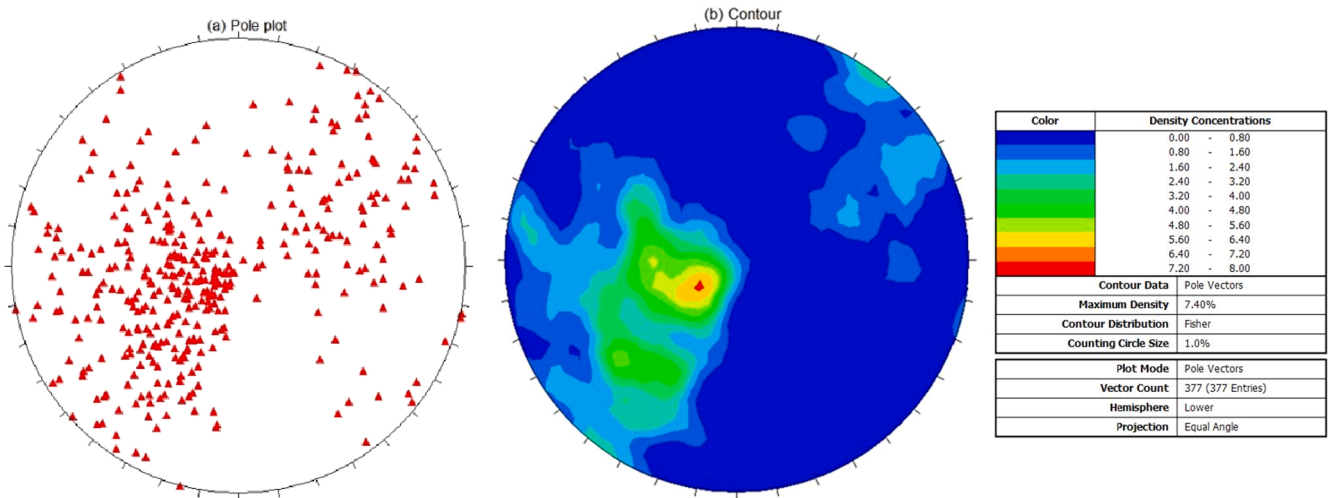**Fig. 2.** Comparison of permeability evolution and experimental data.

Fig. 3. Spatial distribution of NFs orientation for field verification.
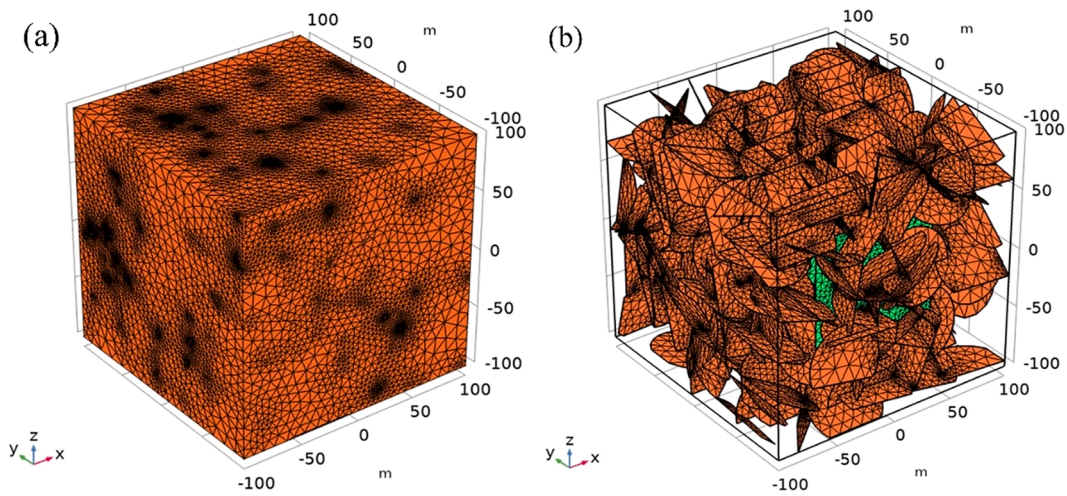

Fig. 4. Mesh views of the model used for field verification of a Haynesville well: (a) tetrahedral mesh diagram of shale matrix; (b) triangular mesh of fracture networks.

Table 2
Primary parameters used in the simulation.

| Parameter	Haynesville reservoir	Base case	Unit
Reservoir dimensions	$200 \times 200 \times 200$	$200 \times 200 \times 200$	m
Original pressure	60	20.34	MPa
Temperature	352	352	K
Bottom hole pressure	20	2	MPa
Viscosity of gas	2×10^{-5}	2×10^{-5}	Pa·s
Possion's ratio	0.2	0.2	–
Langmuir pressure	15×10^{6}	15×10^{6}	Pa
Langmuir volume	2.5×10^{-3}	2.5×10^{-3}	m^3/kg
Langmuir strain constant	0.002	0.002	–
Initial porosity OM	0.05	0.05	–
Fractal dimension of OM	2.25	2.15	–
Fractal tortuosity of OM	1.2	1.2	
Minimum pore size of OM	1	1	nm
Maximum pore size of OM	50	100	nm
Biot coefficient of OM	0.6	0.6	
Compressibility of OM	7.5×10^{-10}	7.5×10^{-10}	Pa^{-1}
Bulk moduls of OM	50	50	GPa
Initial porosity of IOM	0.08	0.08	–
Fractal dimension of IOM	2.35	2.25	–
Fractal tortuosity of IOM	1.2	1.2	–
Minimum pore size of IOM	2	3	nm
Maximum pore size of IOM	200	300	nm
Biot coefficient of IOM	0.7	0.7	–
Compressibility of IOM	4.5×10^{-10}	4.5×10^{-10}	Pa^{-1}
Bulk moduls of IOM	15	15	GPa
Number of NFs	377	50	–
Number of HFs	6	5	–
Initial NF permeability	5	20	mD
Compressibility of NF	5×10^{-9} w	5×10^{-9}	Pa^{-1}
HF width	0.003	0.001	m
HF spacing	30	20	m
Initial HF permeability	200	500	mD
Compressibility of HF	1×10^{-9}	1×10^{-9}	Pa^{-1}
Length of HF	100	40	m
Height of HF	100	40	m
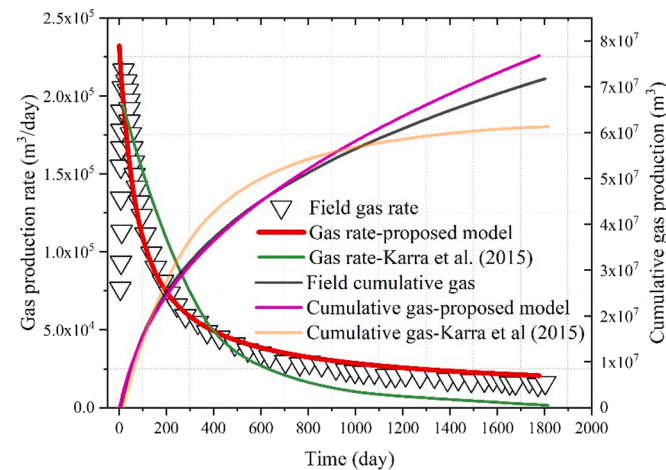
Fig. 5. Comparison between the field data and the simulation results.

without NFs produces the minimum gas volume, with 34% of the base case. By contrast, the remaining three scenarios show almost the same volume, with 4.85×10^6 m^3. When the production time was 1000 days, the cumulative production of the base case reaches 1.17×10 m^3. However, when geomechanics was neglected, the volume increased by 4%, which was attributed to the fact that consideration of geomechanics compromised the permeability. Moreover, it can be seen in Fig. 10 that, when gas adsorption and NFs were not incorporated, the cumulative gas production decreased by 12% and 56%, respectively.

5.2. Evolutions of matrix and fracture permeability

The evolutions of permeability and reservoir pressure were investigated for the base case. The monitoring point for the shale matrix is A (10 m, 10 m, 10 m). At the same time, the probing material point for HF is B (10 m, 20 m, 10 m). The probing point for the NF is the centre point for the No. 5 fracture plane C (-21, 23, −36). Pressure drawdown induced variation in the effective stress and the flow regime, both of which affected the dynamic evolution of the permeability. As shown in Fig. 11(a), the OM permeability scaled up with production time, increasing from 6.9 to 8.3 nD, increasing by 20%. Despite the rising effective stress compacting the shale matrix and reducing the porosity and MPD, the increased Knudsen diffusion and surface diffusion enhanced the apparent permeability. By contrast, for the IOM, permeability fell at the beginning before it rebounds. Fig. 11(b) compared the evolutions of OM and IOM pressure. It can be observed that IOM pressure declined rapidly followed by the OM pressure. When the production time reaches 1000 days, the OM pressure and IOM pressure were 7 MPa and 5 MPa, respectively. As shown in Fig. 11(c), both NF permeability and HF permeability decreased subtly, but the NF permeability decreased more significantly because of smaller compressibility, with an 8% reduction at the production time of 1000 days.

The evolution of the IOM permeability ratio was further investigated under four scenarios with different MPDs, as shown in Fig. 12. From Fig. 12(a), it can be seen that, when the MPD was 100, 200, 300 and 500 nm, the IOM permeability first declined and then rebounded. The decline in permeability can be explained as the effect of effective stress. However, with decreasing pore pressure, the slip flow effect gradually dominated the evolution of the permeability, causing an increase in permeability in the later stages. When the pore pressure was fixed, the larger MPD indicated stronger slip flow effects and a more significant rebound. For the scenario with an MPD of 100 nm, the permeability almost increased monotonously. The reason for this phenomenon is that the impact of the slip flow outweighed the effective stress from the very beginning. Therefore, the upper and lower boundaries of the permeability evolution could be determined based on the spectrum of MPDs. Under the condition of constant confining pressure, our previous study demonstrated that the experimental data scattered between the upper and lower boundaries (Shi et al., 2019). Our model can explain the diversity of the data distribution. It can be concluded that the evolution of IOM permeability is highly dependent on the value of MPD. Characterization of the PSD is essential in evaluating the variation in permeability during gas depletion.

MPD and fractal dimension are critical parameters influencing the apparent permeability of the shale matrix. Dynamic change in the effective stress can induce variations in MPD and fractal dimensions. The changes in these parameters in OM and IOM were compared, as shown in Fig. 12 (b). It can be seen that the MPD in the IOM exhibited a greater reduction than in the OM, decreasing from 300 nm to 296 nm. By contrast, the MPD in the OM only experienced a 0.5% reduction. The reason for the lesser decline in MPD of OM is that the gas desorption-induced pore shrinkage partly offsets the compacting effect caused by the effective stress. Both of the fractal dimensions of OM and IOM witnessed tiny reductions. The gap in reduction percentage can be attributed to the diverse compressibility.

5.3. Evolutions of geomechanical factors

Fig. 13 shows the spatial and temporal distributions of Von Mise stress, volumetric strain and sorption-induced strain, respectively. Maximum Von Mise stress was found at the at the right corner of the horizontal plane. The region at the right corner of the horizontal plane of the model was affected by both stress and the fixed boundaries, and therefore subject to normal and shear stresses along all three coordinate axes. The stresses in different directions may affect each other, leading to the maximum von Mises stress in that region. It can be observed that
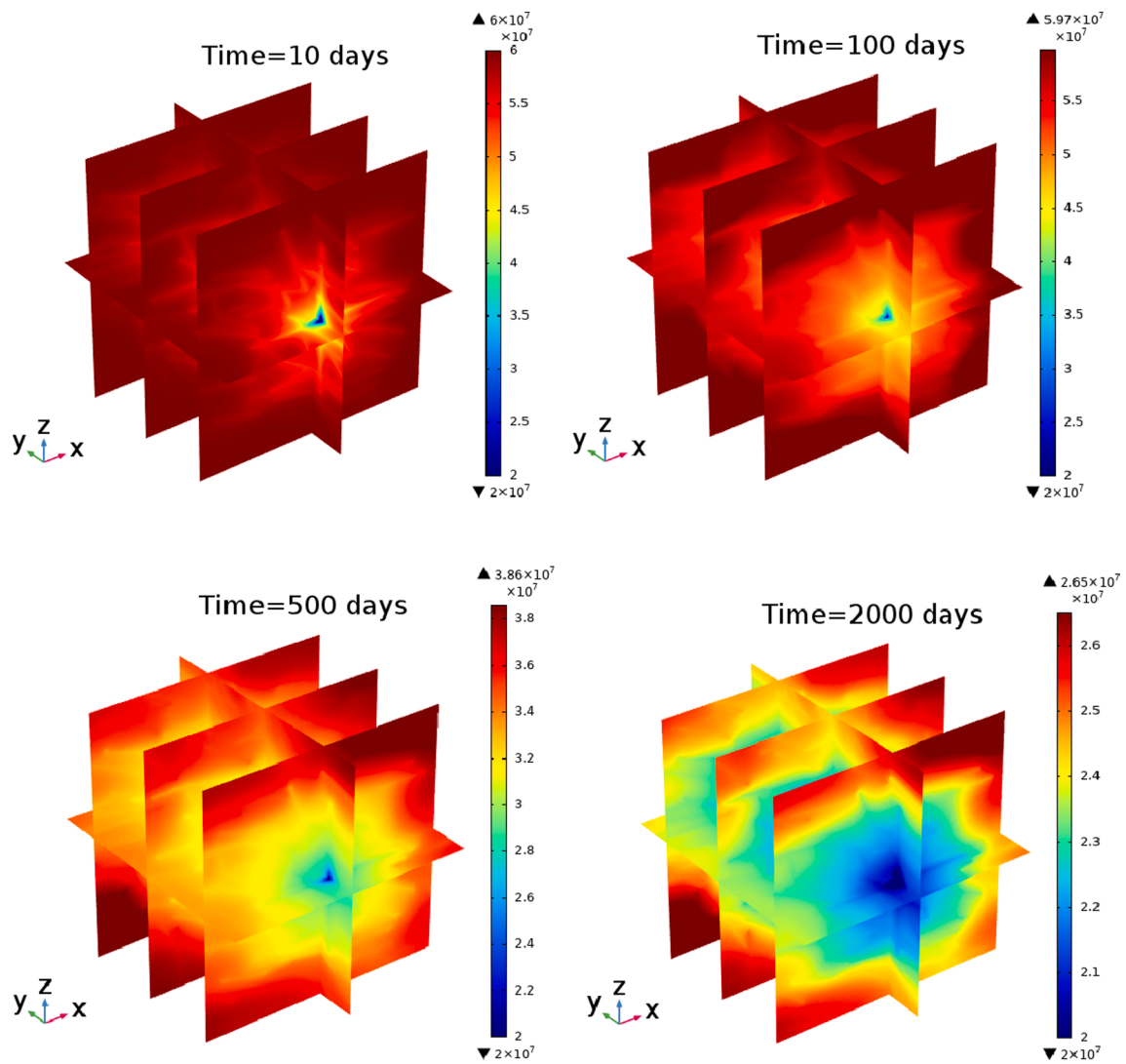
Fig. 6. Slice maps of the matrix pressure when the production time is 10 days, 100 days, 500 days and 2000 days.
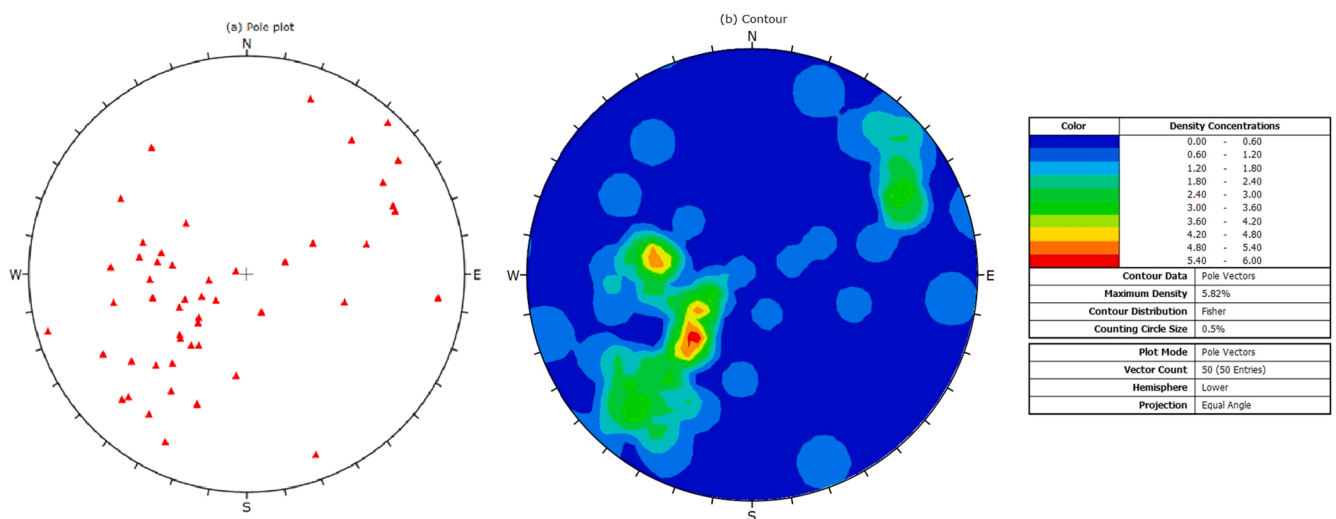

Fig. 7. Spatial distribution of NFs orientation for base case.
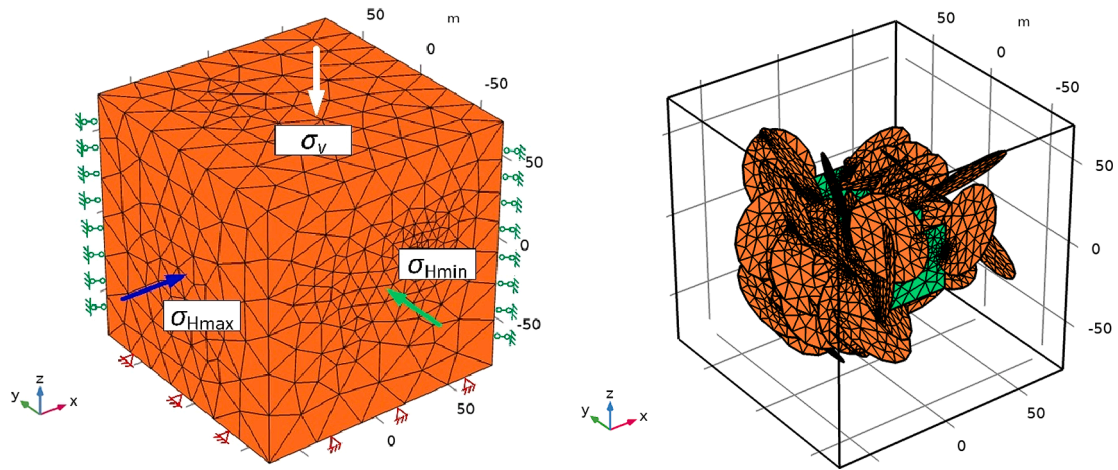
Fig. 8. Mesh views of the model used for base case: (a) tetrahedral mesh diagram of shale matrix; (b) triangular mesh diagram of HF and NF networks.
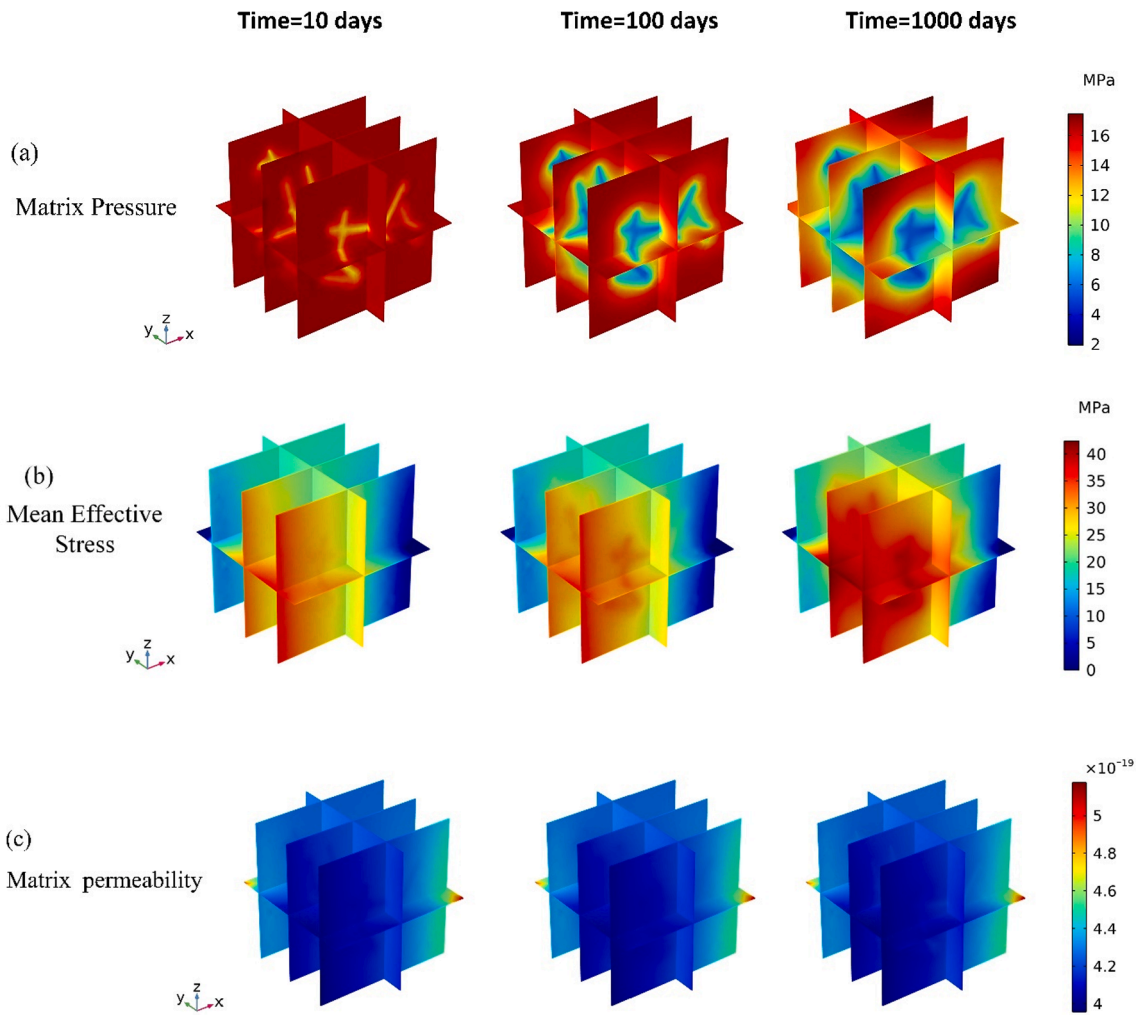

Fig. 9. (a) Evolution of IOM pressure; (b) Variation of mean effective stress; (c) Permeability evolution of IOM of the base case.

the stress concentration occurred in the high-stress zone, which was consistent with the discussion in Fig. 9. Consequently, the volumetric strain in this region reaches 0.0002, nearly doubling the value of the low-stress region. As shown in Fig. 13 (c), the sorption-induced strain was proportional to the evolution of reservoir pressure. When the production time was 1000 days, the sorption strain circling the fractures

decreased from 0.0016 to 0.0011. To further illustrate the impacts of a fracture network on the evolution of effective stress, we selected two cut lines, line A (X = 0, Z = 0) which is perpendicular to the HFs and line B (X = 0, Y = 0) which is parallel to the HFs, to showcase the stress evolution in the simulation model. The locations of line A and line B are displayed in Fig. 14. The evolutions of effective stress (σ_e) from 100 days
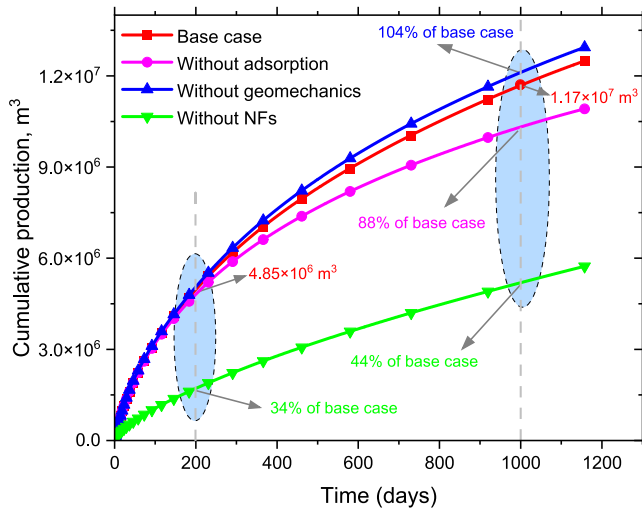
Fig. 10. Comparison of cumulative production from various scenarios.

and 1000 days are presented in Fig. 15. Fig. 15 (a) shows the evolution of the effective stress of line A. It can be observed that the effective stress along the cut line increases when the production time increases from 100 days to 1000 days. Besides, the effective stress spikes in the fracture plane due to the lower pressure. For the line parallel to and through HF, the effective stress in the middle region is higher than on the two sides. Therefore, the presence of fracture networks results in the periodical change spatially.

5.4. Impacts of fractal parameters on productivity

According to the result of Section 5.2, the MPD substantially affects IOM permeability. To reveal the associated implications of MPD on gas production, four sets of MPD (100, 200, 300 and 500 nm) were employed in simulations. Fig. 16(a) presents the evolution of cumulative gas production for these. It can be seen that, when production time is fixed, larger MPD indicated higher cumulative gas production because of greater apparent permeability. It was also found that, when the production time was 1000 days, the cumulative production for $h_{maxi0} = 500 nm$ increased by 25%. By contrast, when the MPD decreased to 100
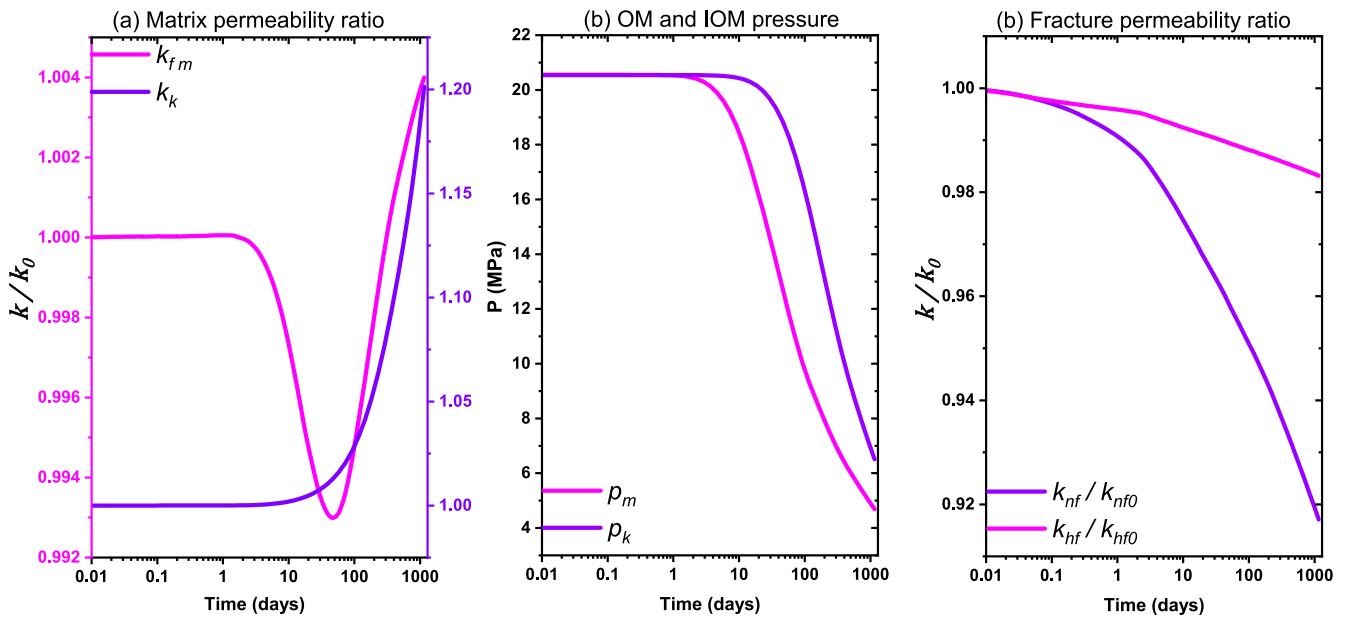

Fig. 11. Evolution of variables for the base case in the monitoring point (10 m, 10 m, 10 m) (a) permeability ratios for OM and IOM; (b) profiles of pressures in OM and IOM; (c) permeability ratios for NF and HF.
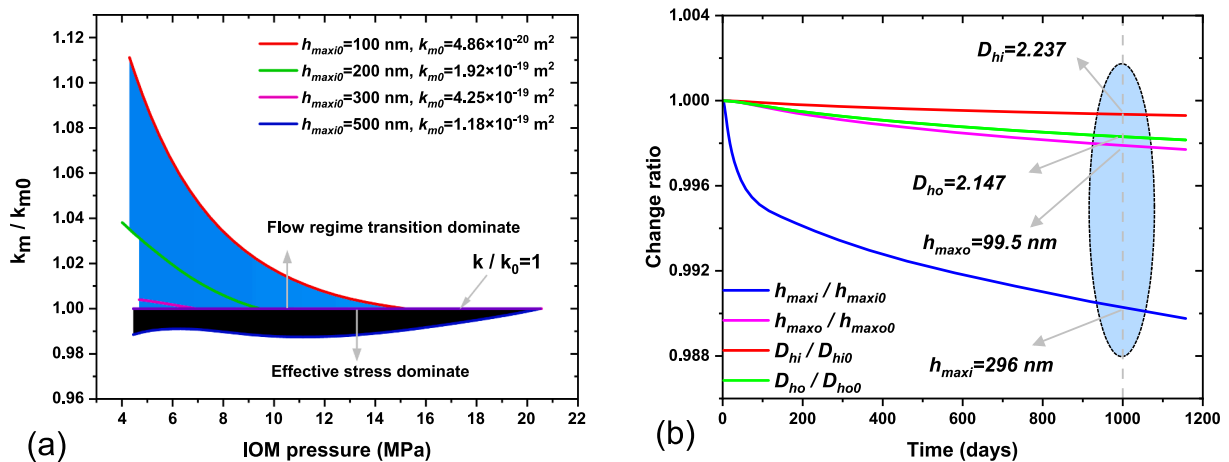

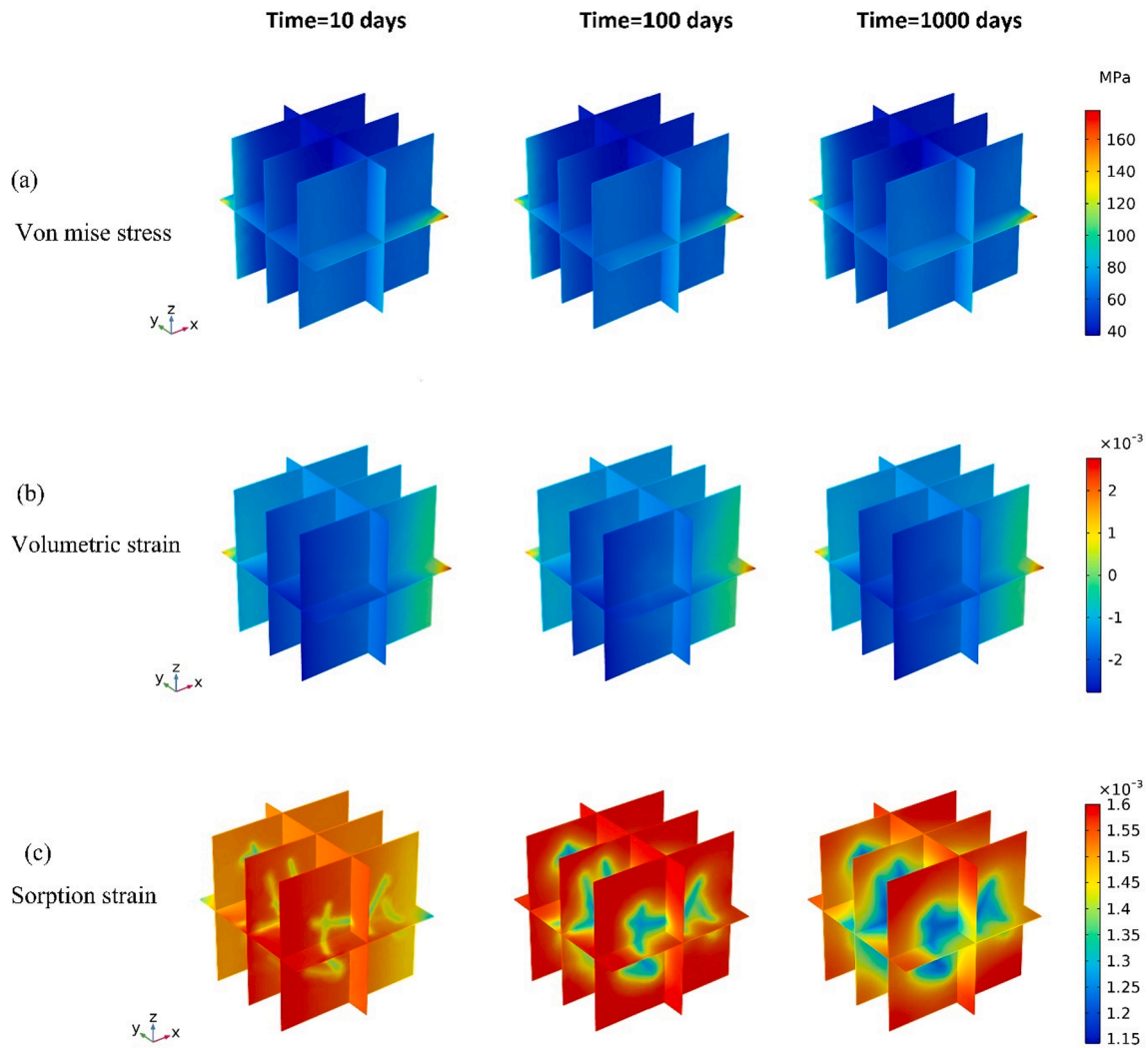**Fig. 12.** Evolutions of IOM permeability for various MPD.

Time=10 days   **Time=100 days**   **Time=1000 days**

(a)

Von mise stress

(b)

Volumetric strain

(c)

Sorption strain

Fig. 13. (a) Evolution of Von Mise stress; (b) Volumetric strain evolution; (c) Sorption-induced strain evolution.
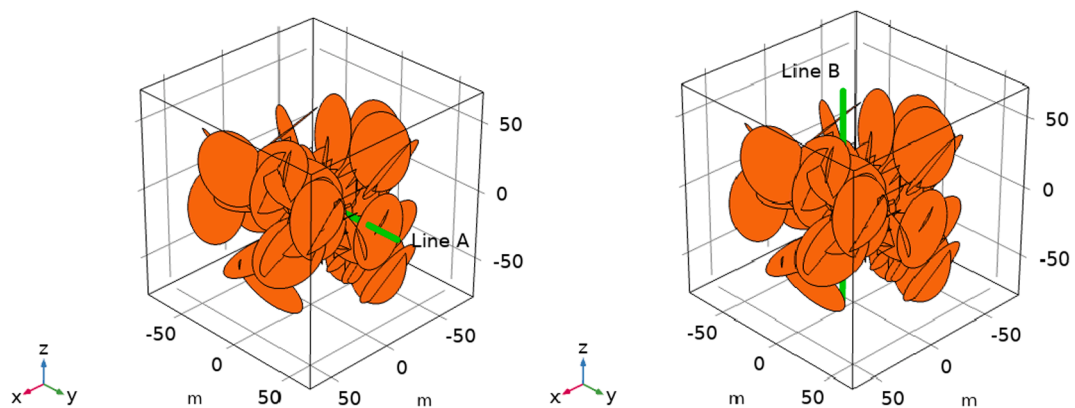
Fig. 14. Schematic illustration of Line A and Line B in the geometry model.

and 200 nm, the cumulative production reduced to 56% and 82% of the base case.

Tortuosity is another crucial parameter that affects permeability in fractal theory. A greater fractal dimension of tortuosity indicates a longer flow length and higher flow resistance. Four cases of the fractal dimension of IOM tortuosity—$D_{Ti} = 1.2$, $D_{Ti} = 1.4$, $D_{Ti} = 1.6$ and $D_{Ti} = 1.8$—were selected to investigate their influence on cumulative gas

production. There was a negative relationship between tortuosity and cumulative gas production and gas production rate. As shown in Fig. 16 (b), the fractal dimension of the tortuosity exhibited a marked effect on the evolution of cumulative gas production, particularly between 100 and 1000 days when the matrix permeability dominated the gas production rate. When the production time was 1000 days, the cumulative gas values for $D_{Ti} = 1.4$, $D_{Ti} = 1.6$ and $D_{Ti} = 1.8$ dropped to 86%, 74%
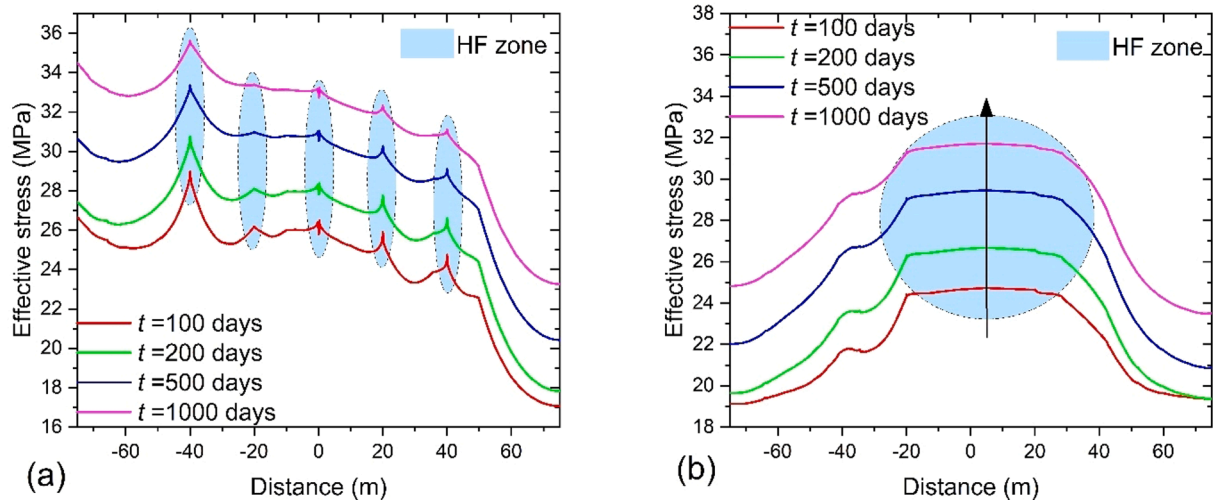
Fig. 15. Evolutions of effective stress for the cut line at different directions (a) perpendicular to the HF (Line A); (b) parallel to the HF plane (Line B).
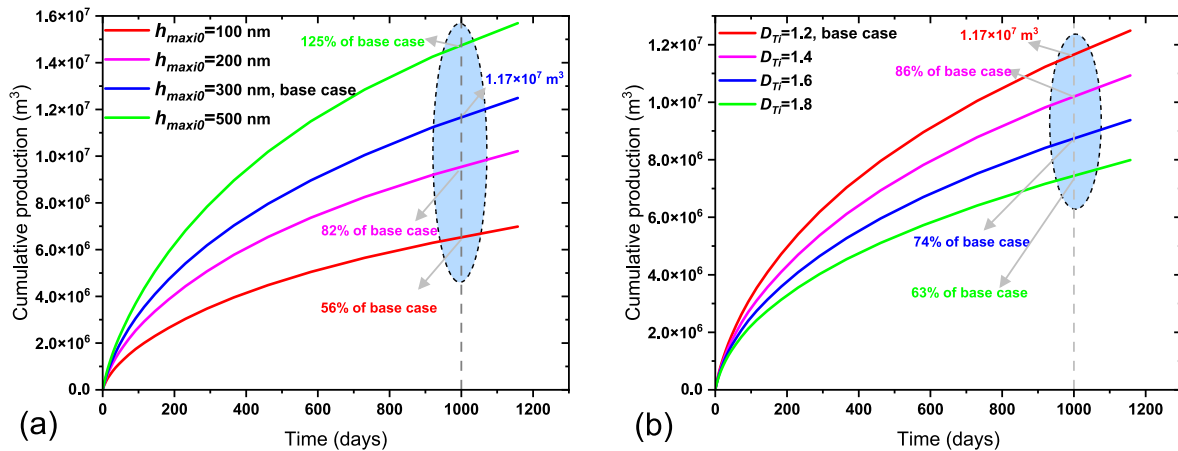

Fig. 16. Impacts of MPD and tortuosity for shale matrix on cumulative gas production.

and 63% of the base case, respectively. It can be concluded that the large tortuosity or complex percolation pathway of shale matrix pores decreases gas production by compromising the matrix permeability.

5.5. Impacts of fracture connectivity on productivity

Fracture connectivity is a dominant indicator in evaluating the conductivity of a reservoir. It is concurrently determined by the fracture size, density and orientation. We maintained the fracture size and density as constants and set different fracture orientations by changing the dispersion coefficient of the Fisher distribution (K). The probability density function of per unit angular area for the angle θ is expressed as (Fisher, 1953):

$$f(\theta) = \frac{K\sin\theta e^{K\cos\theta}}{e^{K} - e^{-K}} \tag{24}$$

The dip angle and direction were simultaneously adjusted. The Fisher distribution coefficient was set as 1 (base case), 5, 15 and 30. Fig. 17 presents the statistical data of intersection lines for the fracture network generated for the different Fisher coefficients. For the four cases, it can be observed that there were 323, 142, 100 and 79 intersection lines. We found that the number of intersection lines decreased with increasing the Fisher coefficient, but the average intersection length declined.

Based on the fractures generated using different distribution

schemes, the corresponding cumulative gas production was investigated. Fig. 18 shows the profiles of cumulative gas production for the four cases of changing Fisher coefficients. It can be seen that when K increased, cumulative gas production declined when the production time was constant. The reason for this is that the higher K indicated weaker connectivity in the NFs because the number of intersection lines between the NFs decreased. When the production time was 1000 days, the cumulative gas production for the base case was 1.17×10^7 m^3. When the K increased to K = 5, K = 15 and K = 30, the cumulative production decreased to 91%, 80% and 72% of the base value, respectively. The total fracture surface volume, P_{32}, is extensively used to characterize fracture connectivity (Dershowitz and Herda, 1992; Maillot et al., 2016; Makedonska et al., 2020b). However, in this study, the fracture size and number for the three cases were kept constant, which would imply that P_{32} would remain constant. Therefore, it is essential to evaluate the fracture connectivity using both the fracture size and the number of intersection lines.

5.6. Impacts of hydraulic fracture patterns on productivity

Fracture aperture directly determines fracture permeability. During shale gas production, a decline in pore pressure can induce fracture closure, which is detrimental to gas recovery (Zhang and Emami-Meybodi, 2020; Zhang et al., 2019). To reveal the specific impacts on gas production rate, four cases of HF apertures (from 0.1 mm to 0.7 mm)
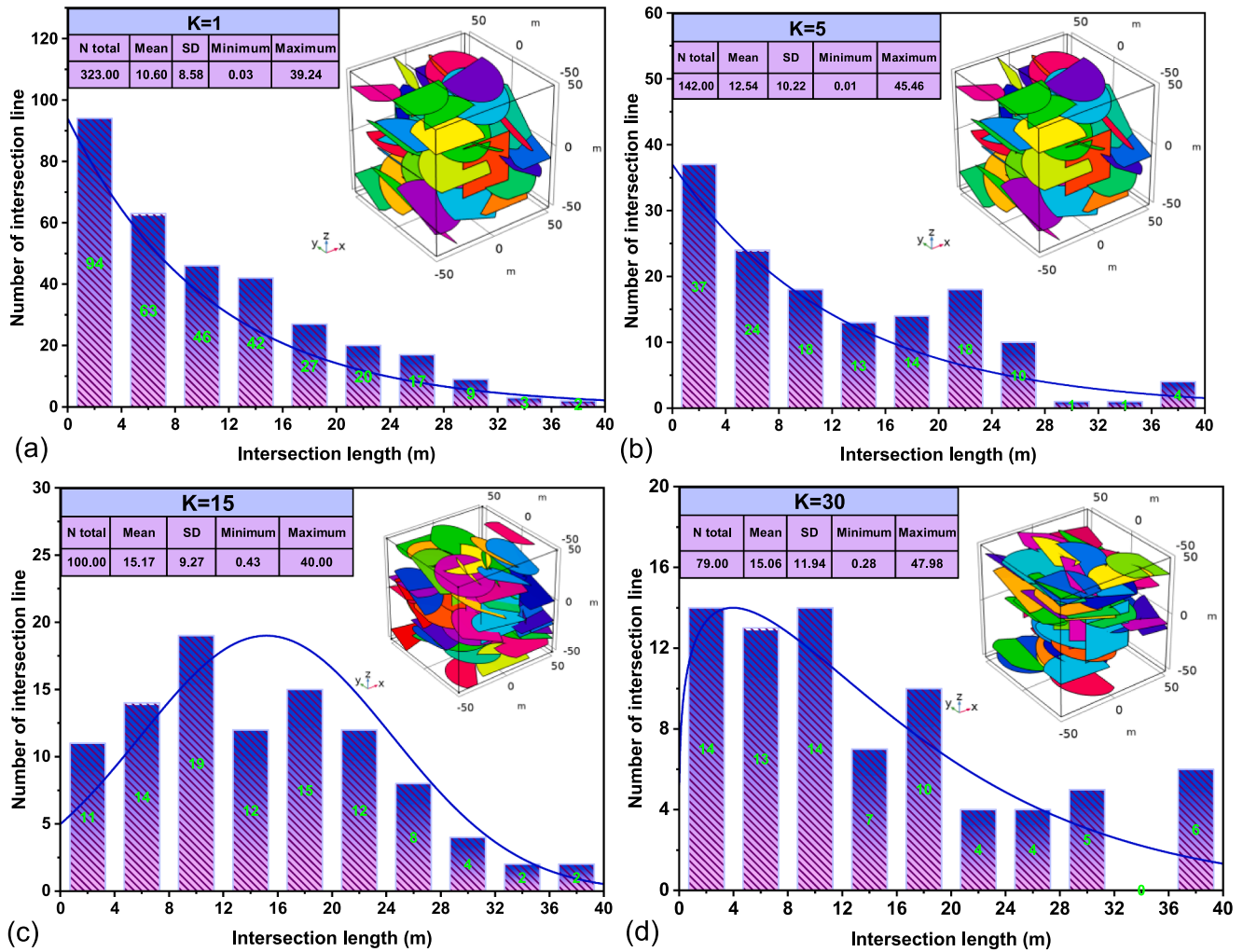
Fig. 17. Statistical distribution of intersection line for 3D discrete fracture model with different Fisher coefficients: (a) K = 1 (base case), (b) K = 5, (c) K = 15 and (d) K = 30.
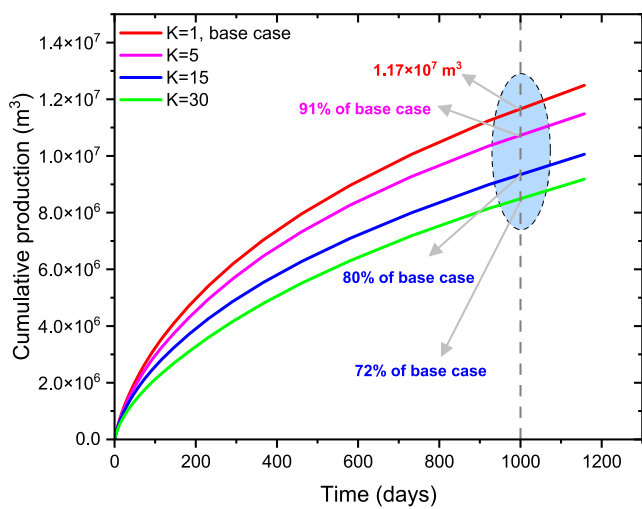

Fig. 18. Impacts of NF connectivity on gas production.

were investigated. Fig. 19(a) shows the changes in the corresponding cumulative gas production with time. The gas production for the base case at 1000 days was 1.17×10^7 m³. When the aperture increased to 0.7 mm, the cumulative production was elevated by 3%. However, for

the cases with apertures equal to 0.3 mm and 0.1 mm, the cumulative gas production decreased to 94% and 78% of the base value. The comparisons between various cases demonstrate that the growth of fracture aperture can enhance the production rate, but the increasing magnitude shows a downward trend.

The configuration of HFs directly determines the size of stimulated reservoir volume, thereby altering the gas production rate. Four groups with diverse numbers of HF were adopted to investigate their associated impacts on gas production. Fig. 19(b) illustrates the evolution of cumulative gas production for these, from which it can be seen that the number of HF had a significant effect on the gas production rate. More HF planes produced higher cumulative gas production. When the hydro-fracturing adopted a seven-HF pattern, the cumulative production increased by 7% more than the base value. However, for the three-HF and single HF plane, the corresponding cumulative gas production witnessed a 15% and 44% decline, respectively. HF pattern should be developed based on the targeted production and fracturing cost because the influence of HF amounts attenuates when the reservoir has a high density of NF and fracture connectivity.

6. Conclusions

In this study, we developed a 3D dual-fractal permeability-discrete fracture model to investigate the impacts of fractal parameters and fracture properties on permeability and gas production, with effective
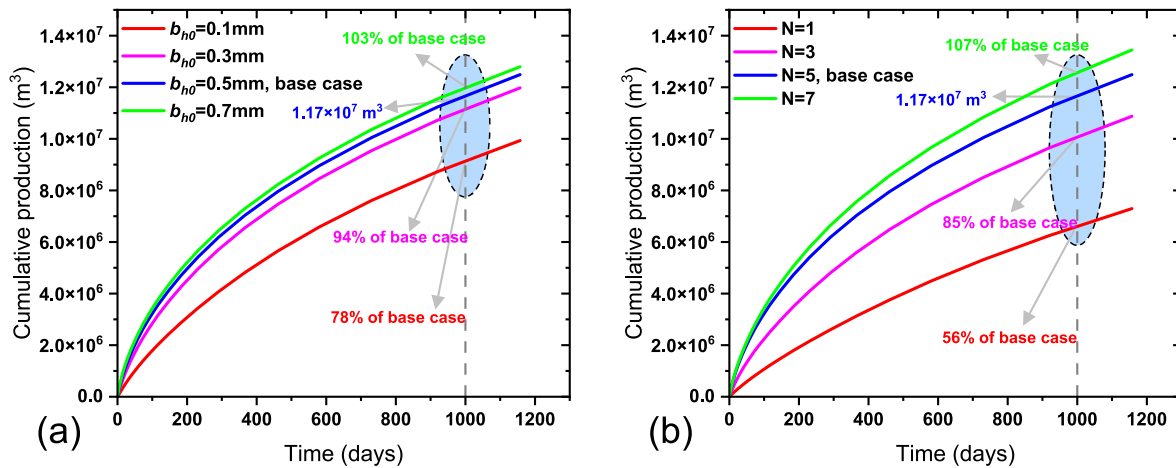
Fig. 19. Impact of HF patterns on cumulative gas production (a) diverse fracture apertures; (b) various numbers of HF.

stress and gas adsorption being incorporated. The Shale matrix was characterized by a dual-fractal approach, allowing quantitative investigation of the associated impacts of heterogeneous pore structure on shale matrix permeability and gas production at the field scale. Besides, the major fractal parameters and the permeability of fractures were effective stress-dependent, enabling the analysis of pore-elastic effects on structural heterogeneity evolution. Based on the sensitivity analysis, the primary conclusions are:

(1) Fractally-distributed pore structure determines the profile of permeability evolution. The permeability of IOM shows a rebounding trend due to the competitive effects between slip flow and effective stress. Enlarged maximum pore diameter could reinforce the slip flow and elevate permeability.

(2) Maximum pore diameter and tortuosity of IOM have the opposite effects on gas production. Effective stress results in the subtle decreases of fractal dimensions and maximum pore diameter. Pore diameter of IOM shows larger decrease than OM due to the desorption-induced shrinkage.

(3) Fracture patterns plays significant roles in gas production. A smaller Fisher coefficient contributes to more intersection lines and lower average inspection length, indicating higher fracture connectivity and production rate. Moreover, a greater number of hydraulic fracture and wider aperture can increase cumulative production, but the growth magnitudes show a decline trend.

Conflicts of Interest

None.

CRediT authorship contribution statement

Jianwei Tian: Methodology, Investigation, Writing – original draft. **Jishan Liu:** Supervision, Writing – review & editing. **Derek Elsworth:** Supervision, Writing – review & editing. **Yee-Kwong Leong:** Supervision, Conceptualization.

Declaration of Competing Interest

The authors declare that they have no known competing financial interests or personal relationships that could have appeared to influence the work reported in this paper.

Acknowledgement

This work is supported by the Australian Research Council under

References

Almarzooq, A., AlGhamdi, T., Koronfol, S., Dernaika, M., Walls, J., 2014. Shale gas characterization and property determination by digital rock physics. Society of Petroleum Engineers, SPE Saudi Arabia Section Technical Symposium and Exhibition.

Barton, N., Bandis, S., Bakhtar, K., 1985. Strength, deformation and conductivity coupling of rock joints, International journal of rock mechanics and mining sciences & geomechanics abstracts. Elsevier 121–140.

Berkowitz, B., Adler, P.M., 1998. Stereological analysis of fracture network structure in geological formations. J. Geophys. Res. Solid Earth 103 (B7), 15339–15360.

Beskok, A., Karniadakis, G.E., 1999. Report: a model for flows in channels, pipes, and ducts at micro and nano scales. Microscale Thermophys. Eng. 3 (1), 43–77.

Cai, J., Lin, D., Singh, H., Wei, W., Zhou, S., 2018. Shale gas transport model in 3D fractal porous media with variable pore sizes. Mar. Pet. Geol. 98, 437–447.

Cao, P., Liu, J., Leong, Y.-K., 2016a. Combined impact of flow regimes and effective stress on the evolution of shale apparent permeability. Journal of Unconventional Oil and Gas Resources 14, 32–43.

Cao, P., Liu, J., Leong, Y.-K., 2016b. A fully coupled multiscale shale deformation-gas transport model for the evaluation of shale gas extraction. Fuel 178, 103–117.

Chang, Z., Zhao, Y., Hu, Y., Yang, D., 2004. Theoretic and experimental studies on seepage law of single fracture under 3D stresses. Chin. J. Rock Mech. Eng. 23 (4), 620–624.

Chen, L., et al., 2015. Heterogeneity of the Lower Silurian Longmaxi marine shale in the southeast Sichuan Basin of China. Mar. Pet. Geol. 65, 232–246.

Civan, F., 2010. Effective Correlation of Apparent Gas Permeability in Tight Porous Media. Transp. Porous Media 82 (2), 375–384.

Clarkson, C.R., Jensen, J.L., Blasingame, T., 2011. Reservoir Engineering for Unconventional Reservoirs: What Do We Have to Consider?. In: North American Unconventional Gas Conference and Exhibition. Society of Petroleum Engineers, The Woodlands, Texas, USA, p. 45.

Cui, X., Bustin, R.M., 2005. Volumetric strain associated with methane desorption and its impact on coalbed gas production from deep coal seams. AAPG Bull. 89 (9), 1181–1202.

Dershowitz, W.S., Herda, H.H., 1992. Interpretation of fracture spacing and intensity. The 33th us symposium on rock mechanics (USRMS). American Rock Mechanics Association.

Fisher, R.A., 1953. Dispersion on a sphere. Proc. R. Soc. Lond. A 217 (1130), 295–305.

Geng, L., Li, G., Zitha, P., Tian, S., Sheng, M., 2016. A fractal permeability model for shale gas flow through heterogeneous matrix systems. J. Nat. Gas Sci. Eng. 35, 593–604.

Hu, B., Wang, J.G., Zhang, K., Ye, Z., 2020. A new triple-porosity multiscale fractal model for gas transport in fractured shale gas reservoirs. J. Nat. Gas Sci. Eng. 103335.

Huang, T., Guo, X., Chen, F., 2015. Modeling transient flow behavior of a multiscale triple porosity model for shale gas reservoirs. J. Nat. Gas Sci. Eng. 23, 33–46.

Jamison, W., Azad, A., 2017. The hydraulic fracture–natural fracture network configuration in shale reservoirs: Geological limiting factors. J. Pet. Sci. Eng. 159, 205–229.

Javadpour, F., 2009. Nanopores and Apparent Permeability of Gas Flow in Mudrocks (Shales and Siltstone). J. Can. Pet. Technol. 48 (08), 16–21.

Kang, S.M., Fathi, E., Ambrose, R.J., Akkutlu, I.Y., Sigal, R.F., 2011. Carbon dioxide storage capacity of organic-rich shales. SPE J. 16 (04), 842–855.

Karra, S., Makedonska, N., Viswanathan, H.S., Painter, S.L., Hyman, J.D., 2015. Effect of advective flow in fractures and matrix diffusion on natural gas production. Water Resour. Res. 51 (10), 8646–8657.

Lang, P.S., Paluszny, A., Zimmerman, R.W., 2014. Permeability tensor of three-dimensional fractured porous rock and a comparison to trace map predictions. J. Geophys. Res. Solid Earth 119 (8), 6288–6307.

Lei, Q., Latham, J.-P., Tsang, C.-F., 2017. The use of discrete fracture networks for modelling coupled geomechanical and hydrological behaviour of fractured rocks. Comput. Geotechn. 85, 151–176.

Letham, E.A., 2011. Matrix Permeability Measurements of Gas Shales: Gas Slippage and Adsorption as Sources of Systematic Error.

Li, L., et al., 2018. An analysis of stochastic discrete fracture networks on shale gas recovery. J. Pet. Sci. Eng. 167, 78–87.

Li, W., et al., 2021. Stress-dependent fracture permeability measurements and implications for shale gas production. Fuel 290, 119984.

Ma, T., Zhang, K., Shen, W., Guo, C., Xu, H., 2021. Discontinuous and continuous Galerkin methods for compressible single-phase and two-phase flow in fractured porous media. Adv. Water Resour. 156, 104039.

Maillot, J., Davy, P., Le Goc, R., Darcel, C., De Dreuzy, J.-R., 2016. Connectivity, permeability, and channeling in randomly distributed and kinematically defined discrete fracture network models. Water Resour. Res. 52 (11), 8526–8545.

Makedonska, N., Karra, S., Viswanathan, H.S., Guthrie, G.D., 2020a. Role of Interaction between Hydraulic and Natural Fractures on Production. J. Nat. Gas Sci. Eng. 103451.

Makedonska, N., Karra, S., Viswanathan, H.S., Guthrie, G.D., 2020b. Role of interaction between hydraulic and natural fractures on production. J. Nat. Gas Sci. Eng. 82, 103451.

Miller, S.A., 2012. Modeling enhanced geothermal systems and the essential nature of large-scale changes in permeability at the onset of slip. Crustal Permeability 353–362.

Rice, J.R., 1992. Fault stress states, pore pressure distributions, and the weakness of the San Andreas fault. International geophysics. Elsevier 475–503.

Sang, G., Elsworth, D., Miao, X., Mao, X., Wang, J., 2016. Numerical study of a stress dependent triple porosity model for shale gas reservoirs accommodating gas diffusion in kerogen. J. Nat. Gas Sci. Eng. 32, 423–438.

Sheng, M., Li, G., Tian, S., Huang, Z., Chen, L., 2016. A fractal permeability model for shale matrix with multi-scale porous structure. Fractals 24 (01), 1650002.

Shi, J., et al., 2013. Diffusion and flow mechanisms of shale gas through matrix pores and gas production forecasting. SPE unconventional resources conference Canada. Society of Petroleum Engineers.

Shi, J.Q., Durucan, S., 2004. Drawdown Induced Changes in Permeability of Coalbeds: A New Interpretation of the Reservoir Response to Primary Recovery. Transp. Porous Media 56 (1), 1–16.

Shi, R., Liu, J., Elsworth, D., 2019. Mechanistic Analysis of Shale Permeability Evolution Data. In: SPE/AAPG/SEG Unconventional Resources Technology Conference. Unconventional Resources Technology Conference, Denver, Colorado, USA, p. 14.

Tian, J., Liu, J., Elsworth, D., Leong, Y.-K., Li, W., 2023. An effective stress-dependent dual-fractal permeability model for coal considering multiple flow mechanisms. Fuel 334, 126800.

Tian, J., et al., 2022. Shale gas production from reservoirs with hierarchical multiscale structural heterogeneities. J. Pet. Sci. Eng. 208, 109380.

Tian, J., Liu, J., Elsworth, D., Leong, Y.-K., Li, W., Zeng, J., 2019. Dynamic Fractal Permeability Model for Heterogeneous Coalbed Reservoir Considering Multiphysics and Flow Regimes. In: Paper presented at the SPE/AAPG/SEG Unconventional Resources Technology Conference, Denver, Colorado, USA, July 2019. https://doi.org/10.15530/urtec-2019-250.

Tinni, A., et al., 2012. Shale permeability measurements on plugs and crushed samples. SPE Canadian Unconventional Resources' as well. Conference. Society of Petroleum Engineers.

Wang, J., Hu, B., Liu, H., Han, Y., Liu, J., 2018a. Effects of 'soft-hard'compaction and multiscale flow on the shale gas production from a multistage hydraulic fractured horizontal well. J. Pet. Sci. Eng. 170, 873–887.

Wang, P., et al., 2016. Heterogeneity of intergranular, intraparticle and organic pores in Longmaxi shale in Sichuan Basin, South China: Evidence from SEM digital images and fractal and multifractal geometries. Mar. Pet. Geol. 72, 122–138.

Wang, S., et al., 2018b. Apparent permeability model for gas transport in shale reservoirs with nano-scale porous media. J. Nat. Gas Sci. Eng. 55, 508–519.

Wang, W., Shahvali, M., Su, Y., 2015. A semi-analytical fractal model for production from tight oil reservoirs with hydraulically fractured horizontal wells. Fuel 158, 612–618.

Wang, Z., Krupnick, A., 2015. A retrospective review of shale gas development in the United States: What led to the boom? Econ. Energy Environ. Policy 4 (1), 5–18.

Wu, Y., et al., 2019. A comprehensive study on geometric, topological and fractal characterizations of pore systems in low-permeability reservoirs based on SEM, MICP, NMR, and X-ray CT experiments. Mar. Pet. Geol. 103, 12–28.

Yu, W., Sepehrnoori, K., 2014. Simulation of gas desorption and geomechanics effects for unconventional gas reservoirs. Fuel 116, 455–464.

Zhang, F., Emami-Meybodi, H., 2020. Flowback fracture closure of multi-fractured horizontal wells in shale gas reservoirs. J. Pet. Sci. Eng. 186, 106711.

Zhang, H., Liu, J., Elsworth, D., 2008. How sorption-induced matrix deformation affects gas flow in coal seams: a new FE model. Int. J. Rock Mech. Min. Sci. 45 (8), 1226–1236.

Zhang, X., et al., 2019. Pressure–dependent fracture permeability of marine shales in the Northeast Yunnan area, Southern China. Int. J. Coal Geol. 214, 103237.